

Rectifier Integrated Multibeam Luneburg Lens Employing Artificial Dielectric as a Wireless Power Transfer Medium at mm Wave Band

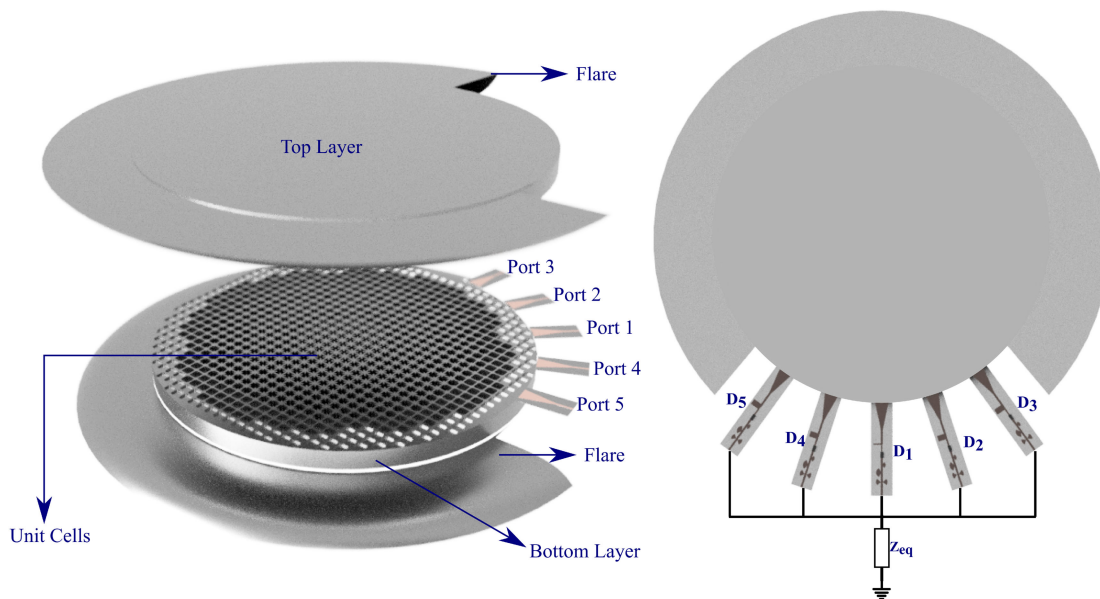
Volume 13, Number 3, June 2021

Sarath Sankar Vinnakota, *Graduate Student Member, IEEE*

Runa Kumari, *Senior Member, IEEE*



Himanshu Meena

Basudev Majumder



DOI: 10.1109/JPHOT.2021.3079180

Rectifier Integrated Multibeam Luneburg Lens Employing Artificial Dielectric as a Wireless Power Transfer Medium at mm Wave Band

Sarath Sankar Vinnakota ¹, *Graduate Student Member, IEEE*,
Runa Kumari,¹ *Senior Member, IEEE*, Himanshu Meena,²
and Basudev Majumder ²

¹Department of Electrical and Electronics Engineering, BITS-Pilani Hyderabad Campus, Telangana 500078, India

²Department of Avionics, IIST Thiruvananthapuram, Department of Space, Government of India, Kerala 695547, India

DOI:10.1109/JPHOT.2021.3079180

This work is licensed under a Creative Commons Attribution 4.0 License. For more information, see <https://creativecommons.org/licenses/by/4.0/>

Manuscript received April 23, 2021; accepted May 5, 2021. Date of publication May 13, 2021; date of current version May 28, 2021. The necessary support for the graduate studies is provided by the University Grants Commission, India (No. 3746, NET-July 2018). This work is carried out within the framework of DST Inspire Faculty Award (IFA17-ENG197). Corresponding author: Sarath Sankar Vinnakota (e-mail: sarath.vinnakota@gmail.com).

Abstract: In this paper, a rectifier integrated Luneburg lens is designed at K band for wireless power transfer (WPT) applications. The lens consists of two metallic layers with a gap of 0.3 mm between them and has been made by employing the glide symmetry technique. A flare is tailored to match the outer impedance of the lens to the free space impedance. Five microstrip tapers are used at intervals of 18° at the periphery of the lens to collect the energy from it. The rectifying circuits are co-designed and are integrated with these five tapered launchers so as to make the entire structure suitable for capturing the transmitted power from the solar power satellite wirelessly, and to convert it to the equivalent voltage. Finally, all the ports are connected with a common load for DC power combining, and the overall performance of the lens integrated rectifier as an energy harvesting system is reported in terms of its power conversion efficiency (PCE).

Index Terms: Electronics, glide symmetry, k-band, luneburg lens, rectenna, sensing, wireless power transfer.

1. Introduction

Lenses are being used in various applications apart from optics such as acoustics [1], radars [2], medical systems [3] etc. More recently the lenses are being explored for potential applications for 5G communication systems [4]. Among the various classes of lens, Luneburg lenses are being implemented for a variety of applications from microwave to optical frequencies [5]–[12]. By selectively rotating the feed along the periphery of the lens a wider range can be scanned. Luneburg lenses require materials that can provide a graded-index (GRIN) and can be implemented using metamaterials or metasurfaces [13]. The refractive index n for a Luneburg lens decreases radially

from the center to the outer surface according to equation (1) [14]

$$\eta = \sqrt{\epsilon_r} = \sqrt{2 - (r/R)^2} \quad (1)$$

where r is the current radius and R is the radius of the lens. The refractive index variation can be achieved by modulating the geometry of the lens. Very recently, higher symmetries like twist, glide, or polar glide symmetry have been explored to design periodic structures such as Luneburg Lenses [15]. When the Luneburg lenses are combined with these symmetries, they can produce wide scan angles over wide band. Glide symmetry is more advantageous since the lenses designed using it, can produce low frequency dispersion and higher equivalent refractive indices over a wide band. Also, as the dependency of the structural parameters is less in glide symmetry, narrow bandwidth problem can be overcome for fixed material properties [16]. Recently in order to avoid the effects of dielectric losses at higher frequencies, all-metal parallel plate waveguide (PPW) structures are being explored to make artificial dielectrics with high values of refractive index [17].

At high frequencies, when the lenses are designed using the dielectrics, the propagation of electromagnetic waves along the surface of the dielectric substrate leads to high dielectric loss and, in some cases, limited bandwidth due to the unsupported TEM waves [13]. To avoid these, alternatively, metals are being considered as they are good conductors with large and imaginary dielectric constant at microwave frequencies and can handle high power too. In [18], a full metal flat ultrawideband Luneburg lens is proposed using two layers of glide symmetry.

In the recent past, wireless power transfer (WPT) and energy harvesting are widely studied to remove the dependency on the use of chemical batteries, thereby going for eco-friendly technologies. The harvesting node of a WPT system consists of a receiver antenna connected to a rectifying circuit, that is capable to convert the incident RF power to DC power. Several such systems have been developed in the last decade in both commercial and ISM bands, particularly, in the sub-6 GHz bands and above the K-band. A significant amount of research is being carried out to realize these systems, known as rectennas where an antenna and a corresponding rectifying circuit have to be co-designed in the same platform. Literature reports various works that paved way for the modern implementations of Wireless power transfer rectennas [19], [20].

Multibeam and directive antennas are preferred when a wider range of areas need to be covered as it becomes relatively difficult for a single antenna to cover multiple directions with high gain. In such cases, the area to be covered is divided into various sectors, and the antennas are designed with high directional gain to cover the sectors [21]. In [22] a driven dipole fed by an integrated balun is used as the antenna with a truncated ground plane reflector. Five such antennas with integrated rectifier circuits designed to operate at 2.45 GHz are used to cover 360° . A cylindrical antenna array with five vertical antenna arrays operating at 2.4 GHz is designed in [23] with each antenna port connected to the single series diode rectifier through a Butler Matrix. A hemispherical multiband coupled-resonator monopole antenna is used in [24] to work at 900 MHz, 1.8 GHz, and 2.4 GHz. More recently, an integrated omnidirectional Vivaldi rectenna array is designed for sensor nodes of the Internet of things [25]. But so far, metasurface inspired multi beam lens as shared WPT medium has not been explored for harvesting the energy from the solar power transmission wirelessly [26]–[28].

It can be inferred from the Frii's transmission equation [29] that a higher aperture area of the receiving antenna results in a higher power to be captured by the antenna, which contributes to the increase in the WPT efficiency [30]. Hence it is desirable that the antennas designed for the WPT applications at higher frequencies have a larger area of the aperture and hence the directivity. Luneburg lenses being directive in nature can become a good alternative for the WPT application as they meet the all design requirements.

Various topologies of the rectifier circuits have been studied widely in the literature like single series, single shunt, voltage doubler, Grienacher rectifier, etc. [31]. Single series topology is the simplest among all of them as only one diode is required for designing the rectifier circuit. Since operating frequency of the design is 24 GHz, it is usually convenient to keep the number of external lumped components as low as possible due to the possible effects of fabrication tolerances on the

final circuit performance. At this frequency, very few works [32]–[38] have been explored for WPT. Most recently, [39] proposed a flexible mm-wave rotman lens on a Liquid Crystal Polymer (LCP) substrate for WPT at 28 GHz. The rotman lens architecture presented, is electrically large and covers a wide area of space to harvest energy for a 5 G wireless power grid for IoT devices.

In this work, a rectifier integrated multibeam 2D graded refractive index (GRIN) Luneburg lens as a WPT medium with DC Combining feature is implemented and investigated numerically to operate at 24 GHz. A single series diode mounted compact feed is co-designed with it at the same frequency. The novelty of the manuscript is twofold. Firstly, the lens consists of all metallic structures which reduces the dielectric loss. For such high frequencies, using dielectrics in design might result in dielectric breakdown. Another noteworthy point is that the proposed structure is having low loss, low cost and can be deployed anywhere as the metal is robust and provides mechanical strength.

Secondly, the diode mounted compact planar feeding arrangement allows seamless integration with the lens. The rectifier integrated feed connected at the one end of the aperture helps to combine the voltage available at each port. The same artificial dielectric metasurface can act as a shared radiating medium or an aperture, which can collect the power from different directions at the same time. To the best of authors' knowledge, till now very few works used dispersive metasurface as 5 G wireless power grid. In addition, at a time 5 ports can share the radiating medium without increasing the overall footprint of the antenna.

The manuscript is organized as follows. The details of the Luneburg lens are presented in Section 2 together with the unit cell analysis and the lens synthesizing. Section 3 reports the rectifier design, its integration with lens and its final performance. Finally the conclusion is drawn in Section 4.

2. Luneburg Lens Design

The Luneburg lens is synthesized in the following sequence. In the first step, the refractive indices are characterized. In the next step, these unit cells are arranged in the form of a GRIN metasurface to realize the entire lens. In the subsequent stage, a suitable flare and rectifier integrated tapered microstrip feeding structure are designed to excite the lens and the performance of the overall structure is tested.

2.1 Unit Cell Design and Analysis

The proposed periodic structure is shown in Fig. 1(a) and (b). The bottom layer of unit cell represented in Fig. 1(a) consists four diagonal extrusions from the four corners of the square unit cell. The variation of the extruded length reduces the phase velocity impacting the effective refractive index of the overall unit cell. This impact can be studied by carrying out the electromagnetic simulations. The periodic boundary condition is applied to the unit cell along the plane tangential to it and it is imposed with an appropriate phase shift on opposite sides of the unit cell corresponding to the propagation constant, β , under investigation. The eigen mode analysis is used to plot the relation between frequency and the propagation constants for Mode 1 and the effective refractive index is extracted. In [17], [40], to change the refractive index, only the height of the unit cell is varied. In the present work, the length of the diagonal extrusions (s) is varied to get the refractive index up to 1.2, and in order to further lower the refractive index, the height of the unit cell (h) is varied while fixing the diagonal corrugation at a fixed value. So, a hybrid unit cell strategy is employed in the present study to cover the full range of Luneburg refractive index profile (1.0 to 1.4). The top layer of the unit cell is obtained by applying the glide symmetry ($(x, y, z) \rightarrow (x + p/2, y + p/2, z)$) on the bottom layer. The gap between the two parallel plates of the lens is $g = 0.3$ mm. The over-all height of the unit cell is limited by the excitation of the higher order PPW (Parallel Plate Waveguide) modes and should be selected less than $\lambda/2$ where λ is the free space wavelength at the highest operating frequency. Once the height is selected, we commence by defining the period (p) of the unit cell. Lower value of p is recommended since it can give closer approximation to an artificial dielectric. But at the same time it increases ohmic losses and increases the demand on manufacturing tolerances. The dimensions used to shape the

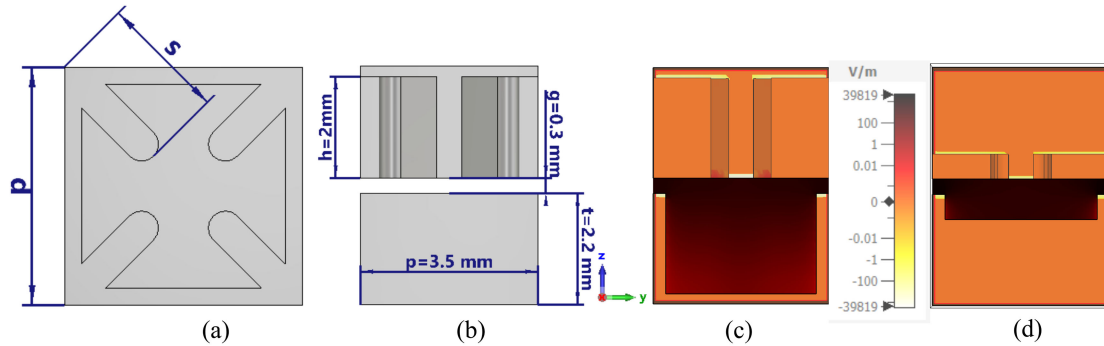


Fig. 1. Geometry of Unit Cell (a) Bottom Layer (b) Top and Bottom Layers; E-field distribution on the unit cell for (c) $s = 1.85$ mm; $h = 2.2$ mm (d) $s = 0.7$ mm; $h = 0.5$ mm.

TABLE I

Refractive Indices and the Corresponding Dimensions of the Final Unit Cells

Layer(j)	1	2	3	4	5	6
n	1.41	1.35	1.26	1.19	1.14	1.05
s_j (mm)	1.85	1.6	1.35	1.1	0.7	0.7
h_j (mm)	2.2	2.2	2.2	2.2	1	0.5

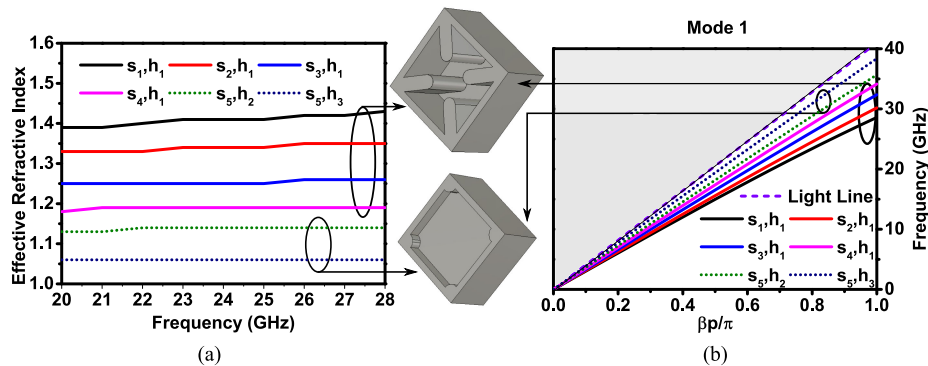


Fig. 2. Eigen Mode Analysis: Variation of (a) effective refractive index (b) mode 1 generated with various unit cell configurations used in the lens design.

various refractive index profiles are shown in Table I. The impact of the diagonal extrusions and the height of the pins on the cross-section of the lens on the refractive indices can be noticed from Fig. 1(c) and (d) along with the Mode graph which is used to calculate the refractive indices.

From Fig. 2(a) and (b) it can be seen that at the absence of the large corrugations and with smaller depth of the unit cell ($h = 0.5$ mm) the phase velocity does not reduce much and it coincides almost with the uniform PPW mode. On the contrary, with the large corrugations and large depth of the unit cell ($h = 2.2$ mm) a relatively high dispersion is observed as compared to the previous cases and the extracted refractive value reaches to 1.4 from 1.05. It is noted that another degree of freedom (DOF), the gap between the two layer (g) does not have much impact on the dispersion. The unit cell for the present study is isotropic in nature and hence its electromagnetic interaction with respect to different direction remains unchanged. Therefore for glide symmetry unit cell design, it is sufficient to investigate the dispersion diagram along the X- direction. The equation showing

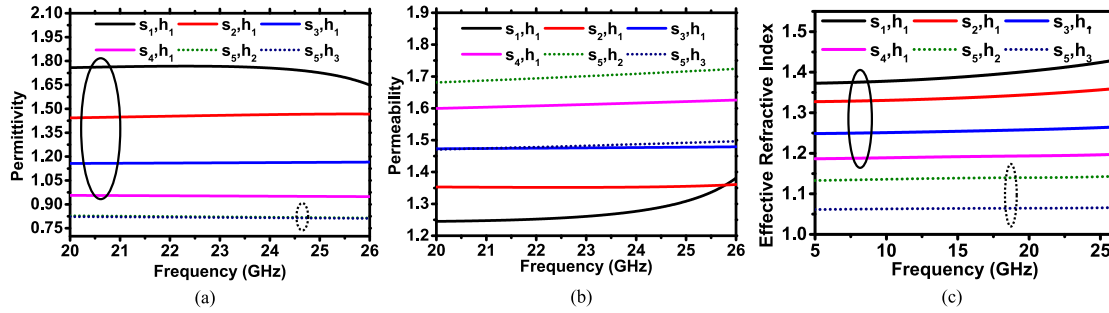


Fig. 3. Transient Analysis: Variation of (a) Permittivity (b) Permeability with the various unit cell configurations used in the lens design (c) Effective refractive index variation with frequency.

the propagation of wave mode in an infinite plane in X-direction is given as [41]

$$\vec{E}(x, y, z) = \sum_{n=-\infty}^{\infty} \vec{E}_n(y, z) \cdot e^{-j\beta_n \cdot \vec{x}} \cdot e^{j\omega t} \quad (2)$$

where $\beta_n(\omega) = \beta(\omega) + n$, β is the phase constant, p is the periodicity of the unit cell. The relation between β and ω is given in the dispersion diagram plot, obtained by eigenmode analysis. For the present case, the variation is given in Fig. 2(b) for various parametric variations.

Fig. 1(c) further verifies the impact of the diagonal extrusions on both the top and the bottom layer in terms of its transverse electric field distribution. When the depth of the unit cell and the diagonal extrusions are large, strong concentration of E field is observed at the transverse plane causing high value of permittivity and refractive index. Reverse trend is observed when the depth and the extrusions are small as shown in Fig. 1(d).

To gain a better understanding about the constitutive parameters corresponding to the excited PPW mode of the lens, the method explained in [42] is employed. The results of which are reported in terms of the permittivity, permeability, and the effective refractive index. The same dimensions of the unit cells studied with the eigen mode analysis are used and are plotted in Fig. 3. From the figure, it can be noted that, when the length (s) of diagonal extrusion is increased with a fixed height, the extracted permittivity decreases but the extracted permeability increases as shown in Fig. 3(a) and (b). The extruded diagonal corrugation gives the surface current in the wall of the unit cell a longer path to traverse which reduces the electrical response (permittivity) of the unit cell and induces a magnetic property (permeability) into it. In the same figure, it can be seen that when s is fixed, and the height is varied, a negligible variation is observed in the extracted permittivity, and only the permeability changes. An interesting observation here is that the permeability tends to decrease, as seen from Fig. 3(b), when the height alone is increased as compared to the increased permeability when only the diagonal corrugations are changed with fixed height. The effective refractive indices obtained from these analysis match with the ones previously calculated from the eigenmode analysis.

2.2 Feeding Geometry and Flare Design

A suitably designed feeding network is necessary to feed the Luneburg lens or to collect the energy from the antenna. To connect the feed, a sectoral arc like portion has been removed from the lens as depicted in the Fig. 6(d). The arc is removed from the best focal point region of the lens so as to make the radiation directive in nature. Too bigger arc can cause degradation in the radiation and too smaller one will defeat the purpose. To ensure the proper working of the feed, shown in Fig. 4(a) it is first tested with the absence of the lens and in a metallic parallel plate mode configuration as shown in Fig. 4(c). The feed is placed in the gap g at the selected point for the proper excitation of the PPW mode. The feed is designed on an RT Duroid substrate of thickness 0.254 mm to

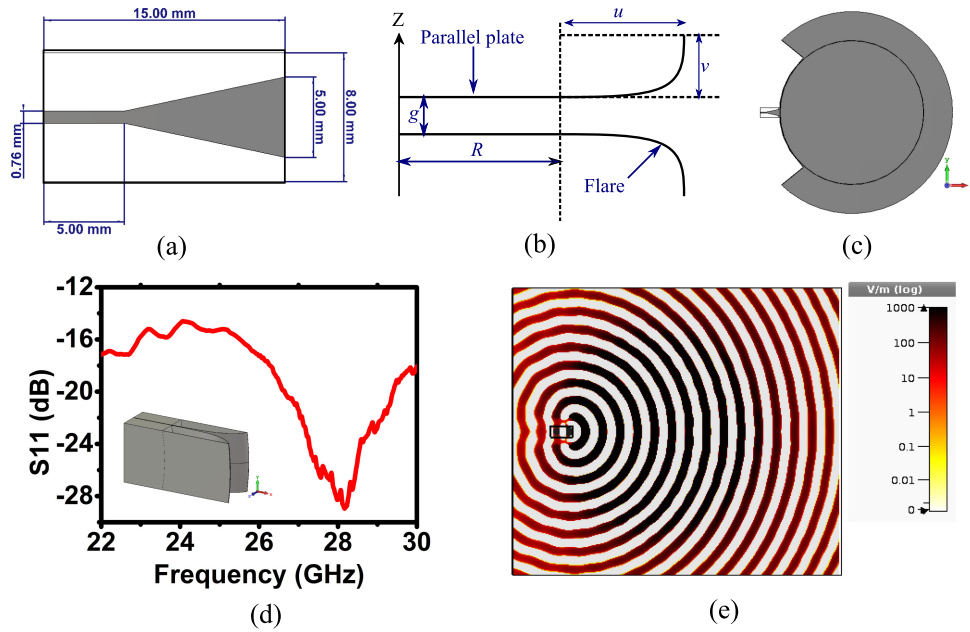


Fig. 4. (a) Feed geometry (b) Flare geometry (c) Parallel plate with flare and feed (d) S_{11} of the structure (e) E-field distribution of the structure at 24 GHz.

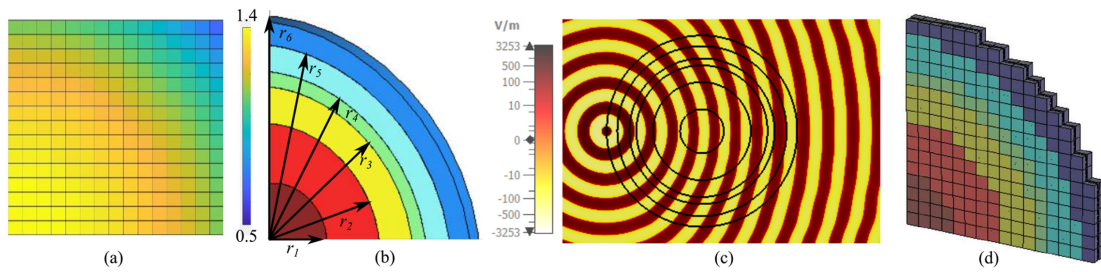


Fig. 5. Refractive index profile of the lens in a quadrant (a) 2D variation (b) Equivalent dielectric realization of lens: $r_1=13$ mm, $r_2=27$ mm, $r_3=37$ mm, $r_4=42$ mm, $r_5=50$ mm, $r_6=59$ mm (c) Simulated electric field distribution of the equivalent lens at 24 GHz (d) Discretized lens construction.

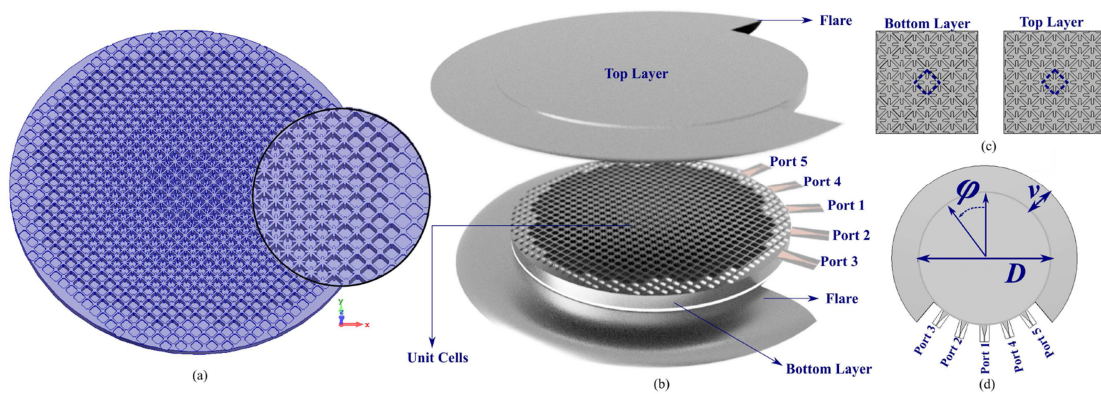


Fig. 6. Realized Antenna (a) Bottom Layer (b) Exploded view of the lens (c) A section of the unit cells (d) Top view of the Lens.

TABLE II
Lens Design Parameters

D	u	v	w	g
118 mm	6 mm	24 mm	5mm	0.3 mm

fit inside the air gap between the top and bottom layers of the lens. The feed consists of a 50 Ω transmission line, where the input SMA connector is connected, followed by a tapered transmission line connected to the parallel plate.

To minimize the elevated reflections from the edge of the PPW due to its abrupt ending, it is matched to that of free space using an exponential flare, and this flare provides a better transition to free space in terms of the impedance matching. The symmetrical exponential flare shown in Fig. 4(b) and inset of Fig. 4(d) consists of a taper of the parallel-plates whose shape exponentially increases. The symmetry axis for the flares is the z-axis, and the $y = g/2$ is the symmetry plane. g is the thickness of the air gap of the lens. The equation for constructing the upper flare for $x \geq 0$ and $z \geq 0$ is [43]

$$z(x) = \begin{cases} g & \text{if } 0 \leq x \leq R, \\ g + u'(e^{\frac{x-R}{w}} - e^{\frac{v}{w}}) & \text{if } R \leq x \leq R + v, \end{cases} \quad (3)$$

where $u' = u(1 - e^{(-v/w)})$ and u, v and w are the geometrical parameters of the flare. These parameters are optimized for use in the required frequency range to $u=6$ mm, $v=24$ mm, and $w=5$ mm. It can be seen from the Fig. 4(d)-4(e) that with the absence of the lens the matched PPW with the designed compact feed can produce good impedance matching along with the spherical electric field distribution.

2.3 Synthesizing the Lens

The feeding and the flare studied above are now integrated with the structure of the lens designed to realize the over-all antenna structure. Some literature reported Horn antennas [40] and tapered waveguide [41] as a feed for the lens. However, feeding with tapered waveguide and horn antennas would require additional and complex waveguide to microstrip transition to integrate the rectifier at the back-end, which would reduce the design flexibility, compactness and add more demanding manufacturing tolerances as far as WPT application is concerned. The ports for the compact feed make an angle of 18 $^\circ$ at the center of the lens. The angle of the feed is selected optimally so that the coupling between the feeding arrangements are less and pattern does not degrade. To design the lens, first the 2D Luneburg refractive index profile is generated as shown in Fig. 5(a). Following this, an equivalent dielectric lens is realized from the extracted material properties from Fig. 3, to obtain the required refractive index and the corresponding dimensions in terms of radius, shown in Fig. 5(b). The simulated E-field at 24 GHz for the equivalent dielectric lens is plotted in Fig. 5(c), which depicts the transformation of spherical wavefront to a planar wavefront. In the next step, the lens is constructed from the unit cell by discretizing the generated RI profile for a single quadrant similar to the procedure shown in [40]. The periodicity p of the unit cell is 3.5 mm and the diameter of the lens D is 118 mm. Therefore, after discretization there are approximately $D/2p = 17$ cells obtained that are placed along the X and Y axis periodically according to refractive index profiles calculated from Fig. 2 and from the dimensions obtained in Fig. 5(b). The area of the quadrant is calculated to be R^2 where $R = D/2$. Then, the lens from the quadrant is expanded using the mirror and circular symmetries to construct the final structure as depicted by the exploded view in Fig. 6(b). The overall design parameters of the antenna are summarized in Table II. After designing the lens, it is simulated in a High-Performance Computing (HPC) environment. From Fig. 7(a), it can be observed that port 1 has a -10 dB impedance bandwidth from 20.5 GHz to 24.5 GHz, covering a band of 4 GHz. Similarly, ports 2 and 4 cover 21.5 GHz to 24.5 GHz, and ports 3 and 5 are consistently below -10 dB for the entire range of interest. The possible cross-talk between

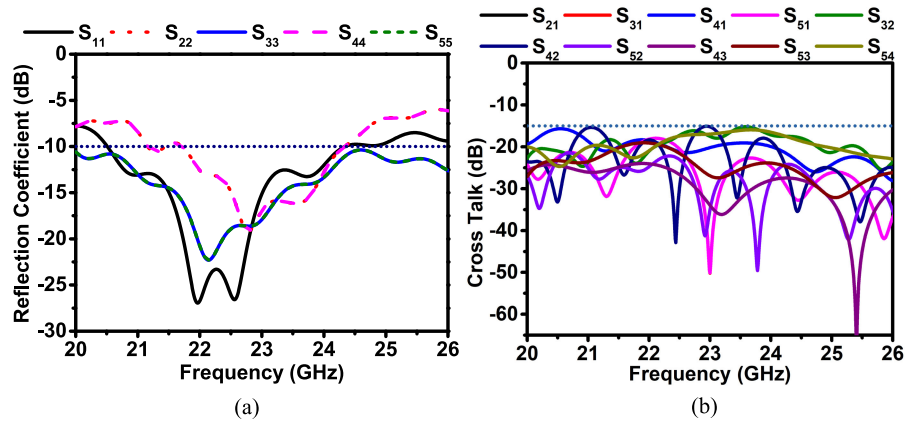


Fig. 7. Antenna results (a) S_{11} vs Frequency (b) Cross talk between any two ports.

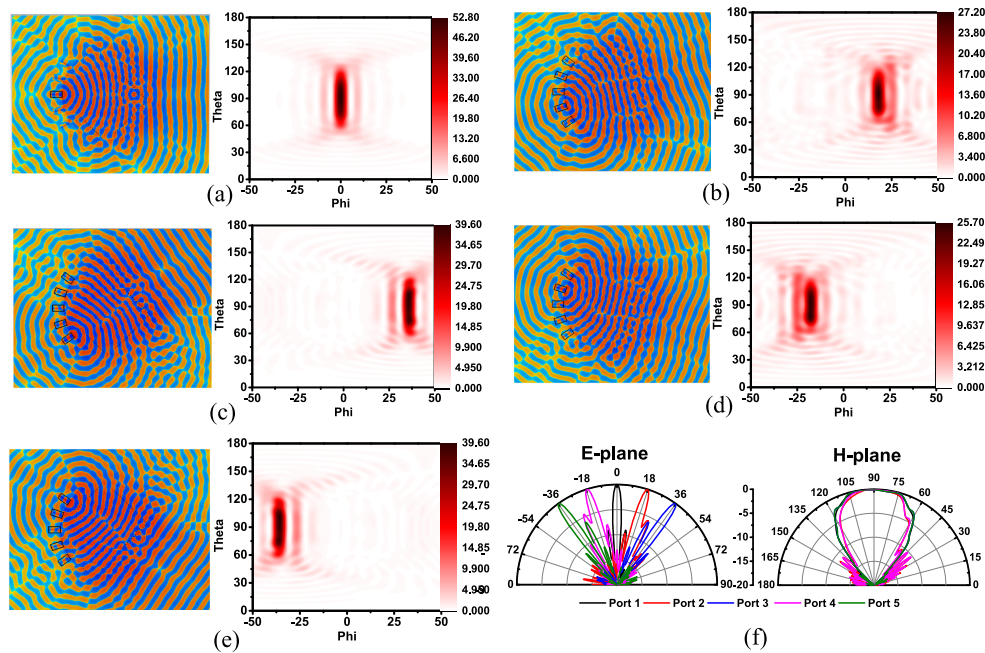


Fig. 8. Electric fields and 2D radiation plots at 24 GHz (a) Port 1 (b) Port 2 (c) Port 3 (d) Port 4 (e) Port 5; (f) Normalized patterns for E plane and H plane.

any two ports is illustrated in Fig. 7(b), and it can be inferred that the cross-talk between any two ports is less than -15 dB for all the possible cases which suits the application. The electric field distribution of the ports with corresponding 2D radiation patterns are shown in Fig. 8(a)–(e) which justifies its directive and beam scanning behaviour. The normalized radiation patterns in both the principle planes (E and H planes) are also shown in Fig. 8, which shows the scanning capability and the fan beam property of the lens in the E plane and H Plane, respectively. The radiation efficiency of the lens is observed above 80% for each of the excitations. The simulated directivity over the impedance bandwidth is observed to be in the range from 15 dB (min) to 17.2 dB (max) for the designed lens.

TABLE III
Antenna Designs for K-Band Rectennas at 24 GHz

Ref.	Antenna Design	Peak Gain(dB)	Max. Bandwidth	S_{11} (dB), Freq	Beam Switching Capability	Max. Size (at 24 GHz)
Proposed Work	Luneburg Lens	17.2 dB(lin: 53)	17.8%	-25, 23 GHz	Yes	6λ
[32] (2020)	Microstrip patch array	13.8 dB	8.51%	-22.5, 23.8 GHz	No	5 λ
[38] (2014)	Cavity backed array	12.6 dB	8%	-19, 25 GHz	Yes	2.5 λ
[44] (2014)	SIW array	15 dB	4.15%	-20, 23.8 GHz	No	6 λ
[45] (2017)	Microstrip patch array	5 dB	3.3%	-24, 24.2 GHz	No	1 λ

The performance of the proposed lens is further compared with some of the other reported antennas designed for rectenna application at K-band in Tab. III. It can be seen that the designed Luneburg lens has a better gain and is capable of receiving multibeam signals as compared to the other reported antennas.

3. Rectenna Design

3.1 Rectifier Configuration and Performance

The main components of a rectenna are the antenna and the rectifying circuit. The rectifying circuit consists of a bandpass filter that acts as an impedance matching network to match the impedance of the antenna to the circuit, a non-linear device, usually, a Schottky diode to rectify the received input power, and a low pass filter (LPF) to filter out the higher-order harmonics generated due to the rectifying diode. The Gallium Arsenide (GaAs) Schottky diodes are preferred over Silicon (Si) schottky diodes for the frequencies above 20 GHz as the junction cutoff frequencies of Si-based diodes, which is around 20 GHz, are further reduced due to the packaging parasitics above 20 GHz. For GaAs diodes, the typical cutoff frequency is above 100 GHz; thus, variation in the cutoff frequency does not have an impact when the diode is used at 24 GHz [30]. For the present application, the Schottky diode selected is MA4E-1317 by MACOM. The package parasitics for the diode are taken from the validated model in [46] for simulation. The efficiency of the rectifier is given by the equation

$$\eta_{\text{PCE}} = \frac{P_{\text{DC}}}{P_{\text{in}}} = \frac{V_{\text{DC}}^2/R_L}{P_{\text{in}}} \quad (4)$$

where P_{DC} is the output DC power, P_{in} is the power at the input of the rectifier, V_{DC} is the output DC voltage and R_L is the load resistance connected at the end of rectifier.

The rectifier circuit is designed and simulated in Keysight ADS on a low loss, 0.254 mm thick Rogers RT Duroid 5880 substrate ($\epsilon_r=2.2$, $\tan\delta = 0.0009$). Following the antenna's design, for the five ports at different angles, five rectifiers have to be designed. The significant difference among these rectifiers is the design of the impedance matching network as the input impedance of the ports connected with the lens vary. For five ports, ideally, five rectifiers have to be designed. However, since ports 2,4 and ports 3,5 are symmetric, their S-parameters are symmetric as well; it is sufficient to design three different matching networks to match the impedance of the rectifier circuit to that of the respective antenna ports.

The rectifier is designed in following steps. At first, the single series rectifier topology is finalized. Although multistage topologies like voltage doubler give a higher DC voltage, the number of via holes required to be drilled on the substrate increases. This causes a significant impact on the circuit performance at higher frequencies. Also, the substrate thickness being around 0.254 mm, drilling via holes and soldering too many components could also have an impact in the form of uneven substrate thickness across the rectifier circuit. This may lead to deviation from the desired circuit performance. A major advantage of the proposed design is the reduced dependency of the lumped components in the design of single series topology. The complete network, including the matching network, is made with distributed realization to remove the challenges due to the presence of lumped elements such as low self resonant frequency, low quality factor, soldering

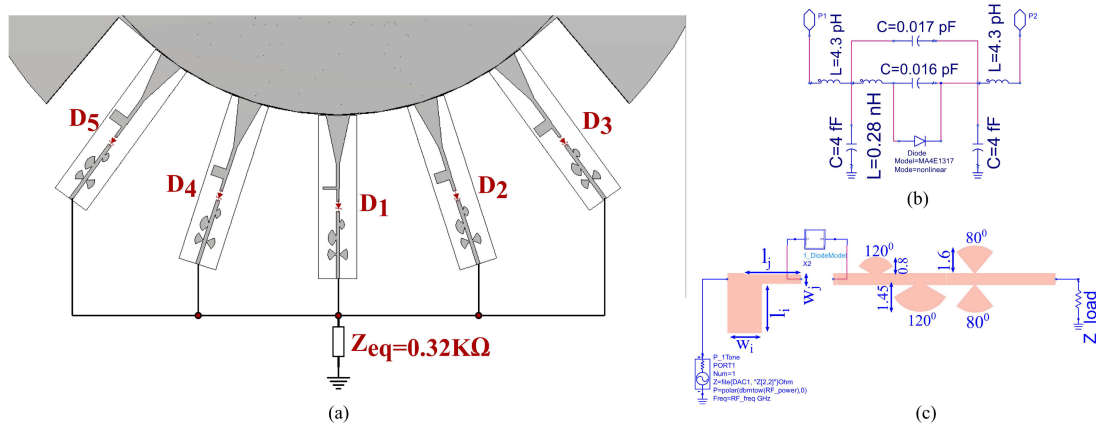


Fig. 9. (a) Realization of rectenna for DC power combining integrated with the feed ports (only a portion of metasurface lens with feed is shown). (b) Diode model including parasitics [46] (c) EM circuit co-simulation layout.

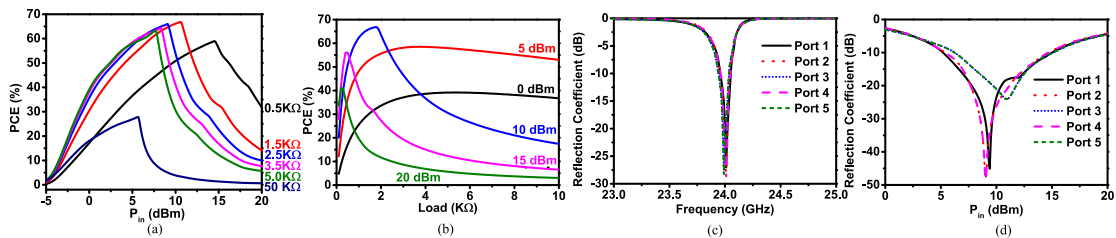


Fig. 10. At 24 GHz (a) Power and the corresponding load calculations for highest possible PCE (b) Load and the corresponding power calculations for highest possible PCE (c) Variation of reflection coefficients for the ports after adding the impedance matching network (d) Variation of reflection coefficients with input power for all the ports.

effects etc. In addition, the chosen diode MA4E1317 does not use any external bias for its operation, further reducing the network complexity. The low pass filter (LPF), required to suppress the higher order harmonic, s has been designed using two radial stubs and a butterfly-shaped stub. The stubs' dimensions along with transmission lines connecting them are tuned to obtain the required filter response at the selected frequency. In the next step, the diode, including parasitics and a load, is connected to the respective ends of the designed LPF. The diode's input port is connected to a frequency domain power source, acting as a substitute to the antenna. The load resistance also impacts the RF-DC efficiency (η_{PCE}) and has to be chosen carefully. The final step is to design an appropriate matching network to each of the ports. For this, the impedance is obtained at the rectifier's input by converting the input reflection coefficient into equivalent Z-parameters. The overall integration of the lens in Fig. 6 with the rectifier ports is shown in Fig. 9(a). The equivalent spice model of the diode including the parasitics is shown in Fig. 9(b). The EM circuit co-simulation layout is shown in 9(c).

3.2 Rectenna Performance

The antenna's S-parameters are converted into Z-parameters and are then imported into ADS using a Data Access Component (DAC). These Z parameters are then associated with the input impedance of the frequency domain power source to perform the CST-ADS co-simulation [47] as seen from Fig. 9(c). Further, the parametric analysis is carried out to determine the most

TABLE IV
Matching Network Dimensions (In MM)

Port	Port Impedance at 24 GHz	w_i	l_i	w_j	l_j
1	$33.07+j*26.09$	0.505	2.67	0.44	2.61
2	$26.17+j*2.19$	2.12	2.64	0.63	2.56
3	$39.79+j*29.28$	2.17	3.01	0.58	2.46
4	$26.17+j*2.19$	2.12	2.64	0.63	2.56
5	$39.79+j*29.28$	2.17	3.01	0.58	2.46

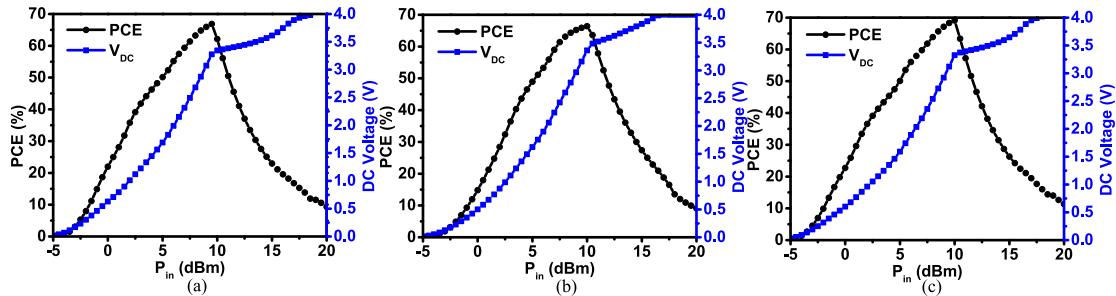


Fig. 11. At 24 GHz, the comparison of PCE and DC voltage with respect to input power for (a) Port 1 (b) Port 2 and Port 4 (c) Port 3 and Port 5.

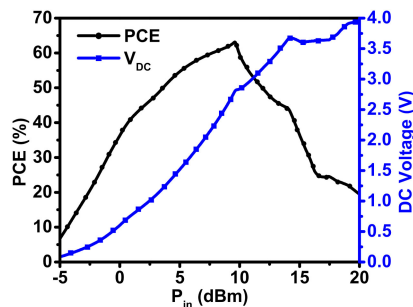


Fig. 12. Graph showing the PCE as well as output DC voltage with varying input power.

appropriate load resistance for the current scenario, and it is found from Fig. 10(a) and (b) that approximately at an input power of 10 dBm the higher PCE is possible when the load impedance Z_L is approximately 1600Ω . These values are now fixed while designing the corresponding matching networks to the lens's individual ports to integrate with the rectifying circuits. The matching network is designed using a simple open stub technique. The overall matching response of the rectenna with respect to frequency and the input power is shown in Fig. 10(c) and (d), respectively. The dimensions of the matching network are presented for the individual ports in Tab. IV. The power conversion efficiencies and the output DC voltages for all the ports after adding the matching network are presented in Fig. 11. It can be inferred that port 1 gives a maximum PCE of 64% with an output voltage of 3.4 V at 10 dBm. The ports 2, 4 produce a peak PCE of 66% with 3.5 V, while ports 3, 5 give PCE of 69% at 10 dBm with an output DC voltage around 3.4 V. So overall for all the individual ports a reasonably good PCE is observed.

3.3 DC Power Combining

The parallel additive DC power combining concept is previously explored in the literature in [48], [49]. The concept is implemented by connecting the output nodes of the individual rectifiers in

TABLE V
Comparison With Published Rectennas At 24 GHz

Ref. (Year)	PCE (Sim.)	DC voltage	P_{in}	Diode	Topology
Proposed Work	63	2.75 V	9.5 dBm	MA4E1317	Single series
[50] (2021)	44.3	-	14.8 dBm	MA4E1317	Voltage doubler
[51] (2021)	54	8 V	13 dBm	Hybrid	2 stage Voltage multiplier
[37] (2020)	12	3 V	10 dBm	MA4E1319	Voltage doubler
[32] (2020)	35	2.5 V	14 dBm	MA4E2054A	Single shunt
[34] (2019)	7.5	-	8 dBm	MA4E1217	Single shunt
[35] (2017)	35.2	-	15 dBm	MA4E1317	Single diode
[38] (2014)	45	1.1 V	18 dBm	MA4E1317	Self biased
[33] (2013)	24	0.6 V	18 dBm	MA4E2502L	Single series
[36] (2011)	54.2	5.6 V	21.14 dBm	MADS01317	Single shunt

parallel and then connecting them to a common load $Z_{eq}=Z_L/5=320 \Omega$. This load and the rectenna share a common DC ground plane. By connecting in such a way, the currents get added up and contribute to increasing the overall average DC power of the rectifier. The voltage, however, remains equal to that of the voltages generated at the terminals of the individual ports. It can be inferred from Fig. 12 that an overall power conversion efficiency of 63% is obtained at an input power of 9.5 dBm at 24 GHz when the rectenna ports are connected in parallel. The performance of the designed rectenna is compared with the state of the art in Tab. V.

4. Conclusion

In this paper, a rectenna is proposed for K-band, using a 2D GRIN Luneburg lens with an all-metal structure. The lens is constructed using two Glide-Symmetric Metasurface layers with a small gap in between. Five tapered waveguide feedings are used to power the lens for multiple directions. The peak gain of the lens is 17.2 dB (52 in linear scale) at port 1 and the gain of the other ports remain between 14 dB and 16 dB. The entire lens is then analyzed for wireless power transfer application in the K-band at 24 GHz in the context of DC power combining concept. The designed rectifying circuit gives a power conversion efficiency (PCE) of 63% at an input power of 9.5 dBm.

Acknowledgment

The authors gratefully acknowledge the computing time provided on the high performance computing facility, Sharanga, at the Birla Institute of Technology and Science - Pilani, Hyderabad Campus. The authors also acknowledge the High Performance Computation facility at IIST Thiruvananthapuram. The authors would also like to acknowledge 3DS for CST Microwave Studio 2021 and Keysight for ADS 2017 for providing the software. The authors would like to thank Dr. Oscar Quevedo-Teruel of KTH Royal Institute of Technology, Stockholm for the technical inputs and helpful discussions. The authors also thank Avinash Kothuru from BITS Pilani Hyderabad campus for his help in improving the figures of the manuscript.

References

- [1] Q. Rong *et al.*, "Ultrasonic sensitivity-improved Fabry–Perot interferometer using acoustic focusing and its application for noncontact imaging," *IEEE Photon. J.*, vol. 9, no. 3, Jun. 2017, Art. no. 6802511.
- [2] J. Yang, C. Huang, J. Song, X. Zhang, X. Xie, and X. Luo, "Metasurface-based lens for antenna gain enhancement and radar cross section reduction," *IEEE Photon. J.*, vol. 11, no. 6, Dec. 2019, Art. no. 4601809.
- [3] D. Lorensen, X. Yang, and D. D. Sampson, "Accurate modeling and design of graded-index fiber probes for optical coherence tomography using the beam propagation method," *IEEE Photon. J.*, vol. 5, no. 2, Apr. 2013, Art. no. 3900015.
- [4] O. Quevedo-Teruel, M. Ebrahimpouri, and F. Ghasemifard, "Lens antennas for 5G communications systems," *IEEE Commun. Mag.*, vol. 56, no. 7, pp. 36–41, Jul. 2018.
- [5] F. Gaufllet and E. Akmansoy, "Graded photonic crystals for luneburg lens," *IEEE Photon. J.*, vol. 8, no. 1, Feb. 2016, Art. no. 2400211.

- [6] Y. Xie *et al.*, "Acoustic imaging with metamaterial luneburg lenses," *Sci. Rep.*, vol. 8, no. 1, pp. 16188(1)–16188(6), Nov. 2018. [Online]. Available: <https://doi.org/10.1038/s41598-018-34581-7>
- [7] Y. L. Loo, Y. Yang, N. Wang, Y. G. Ma, and C. K. Ong, "Broadband microwave luneburg lens made of gradient index metamaterials," *J. Opt. Soc. Amer. A*, vol. 29, no. 4, pp. 426–430, Apr 2012. [Online]. Available: <https://josaa.osa.org/abstract.cfm?URI=josaa-29-4-426>
- [8] S. Tol, F. L. Degertekin, and A. Erturk, "Phononic crystal luneburg lens for omnidirectional elastic wave focusing and energy harvesting," *Appl. Phys. Lett.*, vol. 111, no. 1, pp. 013503-1–013503-5, 2017. [Online]. Available: <https://doi.org/10.1063/1.4991684>
- [9] S. H. Badri and M. M. Gilarlue, "Ultrashort waveguide tapers based on luneburg lens," *J. Opt.*, vol. 21, no. 12, pp. 125802, Nov. 2019. [Online]. Available: <https://doi.org/10.1088/2040-8986/ab4fa3>
- [10] C. Mateo-Segura, A. Dyke, H. Dyke, S. Haq, and Y. Hao, "Flat luneburg lens via transformation optics for directive antenna applications," *IEEE Trans. Antennas Propag.*, vol. 62, no. 4, pp. 1945–1953, Apr. 2014.
- [11] A. D. Falco, S. C. Kehr, and U. Leonhardt, "Luneburg lens in silicon photonics," *Opt. Exp.*, vol. 19, no. 6, pp. 5156–5162, Mar. 2011. [Online]. Available: <https://www.opticsexpress.org/abstract.cfm?URI=oe-19-6-5156>
- [12] A. Demetriadou and Y. Hao, "Slim luneburg lens for antenna applications," *Opt. Exp.*, vol. 19, no. 21, pp. 19925–19934, Oct. 2011. [Online]. Available: <https://www.opticsexpress.org/abstract.cfm?URI=oe-19-21-19925>
- [13] J. A. Dockrey, M. J. Lockyear, S. J. Berry, S. A. R. Horsley, J. R. Sambles, and A. P. Hibbins, "Thin metamaterial luneburg lens for surface waves," *Phys. Rev. B*, vol. 87, pp. 125137-1–125137-5, Mar. 2013. [Online]. Available: <https://link.aps.org/doi/10.1103/PhysRevB.87.125137>
- [14] R. Luneburg, *Mathematical Theory of Optics*. Berkeley, CA, USA: Univ. of California Press, 2021. [Online]. Available: <https://books.google.co.in/books?id=G4ntDwAAQBAJ>
- [15] F. Ghasemifard, M. Norgren, and O. Quevedo-Teruel, "Twist and polar glide symmetries: An additional degree of freedom to control the propagation characteristics of periodic structures," *Sci. Rep.*, vol. 8, no. 1, pp. 11266(1)–11266(7), Jul. 2018. [Online]. Available: <https://doi.org/10.1038/s41598-018-29565-6>
- [16] O. Quevedo-Teruel, Q. Chen, F. Mesa, N. J. G. Fonseca, and G. Valerio, "On the benefits of glide symmetries for microwave devices," *IEEE J. Microw.*, vol. 1, no. 1, pp. 457–469, 2021.
- [17] O. Quevedo-Teruel, J. Miao, M. Mattsson, A. Algaba-Brazalez, M. Johansson, and L. Manholm, "Glide-symmetric fully metallic luneburg lens for 5G communications at ka-band," *IEEE Antennas Wireless Propag. Lett.*, vol. 17, no. 9, pp. 1588–1592, Sep. 2018.
- [18] O. Quevedo-Teruel, M. Ebrahimpouri, and M. Ng Mou Kehn, "Ultrawideband metasurface lenses based on off-shifted opposite layers," *IEEE Antennas Wireless Propag. Lett.*, vol. 15, pp. 484–487, Dec. 2016.
- [19] T. Yoo and K. Chang, "Theoretical and experimental development of 10 and 35 GHz rectennas," *IEEE Trans. Microw. Theory Techn.*, vol. 40, no. 6, pp. 1259–1266, Jun. 1992.
- [20] B. Strassner and K. Chang, "Microwave power transmission: Historical milestones and system components," *Proc. IEEE*, vol. 101, no. 6, pp. 1379–1396, 2013.
- [21] F. Fezai, C. Menudier, M. Thevenot, T. Monediere, and N. Chevalier, "Multidirectional receiving system for RF to dc conversion signal: Application to home automation devices," *IEEE Antennas Propag. Mag.*, vol. 58, no. 3, pp. 22–30, Jun. 2016.
- [22] Y. Chen and J. You, "A scalable and multidirectional rectenna system for rf energy harvesting," *IEEE Trans. Compon. Packag. Manuf. Technol.*, vol. 8, no. 12, pp. 2060–2072, Dec. 2016.
- [23] E. Vandelle, D. H. N. Bui, T. Vuong, G. Ardila, K. Wu, and S. Hemour, "Harvesting ambient RF energy efficiently with optimal angular coverage," *IEEE Trans. Antennas Propag.*, vol. 67, no. 3, pp. 1862–1873, Mar. 2019.
- [24] B. Zhang, J. M. Kovitz, and Y. Rahmat-Samii, "A hemispherical monopole rectenna array for multi-directional, multi-polarization, and multi-band ambient rf energy harvesting," in *Proc. IEEE Int. Symp. Antennas Propag.*, 2016, pp. 603–604.
- [25] C. Song, P. Lu, and S. Shen, "Highly efficient omnidirectional integrated multi-band wireless energy harvesters for compact sensor nodes of Internet-of-Things," *IEEE Trans. Ind. Electron.*, pp. 1–1, 2020.
- [26] P. Koert and J. T. Cha, "Millimeter wave technology for space power beaming," *IEEE Trans. Microw. Theory Techn.*, vol. 40, no. 6, pp. 1251–1258, Jun. 1992.
- [27] J. O. McSpadden and J. C. Mankins, "Space solar power programs and microwave wireless power transmission technology," *IEEE Microw. Mag.*, vol. 3, no. 4, pp. 46–57, Dec. 2002.
- [28] C. T. Rodenbeck *et al.*, "Microwave and millimeter wave power beaming," *IEEE J. Microw.*, vol. 1, no. 1, pp. 229–259, 2021.
- [29] C. Balanis, *Antenna Theory: Analysis and Design, Ser. Jeff Borrow List*. Hoboken, NJ, USA: Wiley, 2005. [Online]. Available: <https://books.google.co.in/books?id=agWwQgAACAAJ>
- [30] M. Wagih, A. S. Weddell, and S. Beeby, "Millimeter-wave power harvesting: A review," *IEEE Open J. Antennas Propag.*, vol. 1, pp. 560–578, Oct. 2020.
- [31] C. R. Valenta and G. D. Durgin, "Harvesting wireless power: Survey of energy-harvester conversion efficiency in far-field, wireless power transfer systems," *IEEE Microw. Mag.*, vol. 15, no. 4, pp. 108–120, Jun. 2014.
- [32] B. T. Malik, V. Doychinov, A. M. Hayajneh, S. A. R. Zaidi, I. D. Robertson, and N. Somjit, "Wireless power transfer system for battery-less sensor nodes," *IEEE Access*, vol. 8, pp. 95878–95887, 2020.
- [33] A. Collado and A. Georgiadis, "24 GHz substrate integrated waveguide (SIW) rectenna for energy harvesting and wireless power transmission," in *Proc. IEEE MTT-S Int. Microw. Symp. Dig.*, 2013, pp. 1–3.
- [34] B. T. Malik *et al.*, "Flexible rectennas for wireless power transfer to wearable sensors at 24 GHz," in *Proc. Research, Invent. Innov. Congr.*, 2019, pp. 1–5.
- [35] S. Daskalakis, J. Kimionis, J. Hester, A. Collado, M. M. Tentzeris, and A. Georgiadis, "Inkjet printed 24 GHz rectenna on paper for millimeter wave identification and wireless power transfer applications," in *Proc. IEEE MTT-S Int. Microw. Workshop Ser. Adv. Mater. Processes RF THz Appl.*, 2017, pp. 1–3.
- [36] N. Shinohara, K. Nishikawa, T. Seki, and K. Hiraga, "Development of 24 GHz rectennas for fixed wireless access," in *Proc. XXXth URSI Gen. Assem. Sci. Symp.*, 2011, pp. 1–4.

- [37] M. Wagih, G. S. Hilton, A. S. Weddell, and S. Beeby, "Broadband millimeter-wave textile-based flexible rectenna for wearable energy harvesting," *IEEE Trans. Microw. Theory Techn.*, vol. 68, no. 11, pp. 4960–4972, Nov. 2020.
- [38] S. Ladan, A. B. Guntupalli, and K. Wu, "A high-efficiency 24 GHz rectenna development towards millimeter-wave energy harvesting and wireless power transmission," *IEEE Trans. Circuits Syst. I*, vol. 61, no. 12, pp. 3358–3366, Dec. 2014.
- [39] A. Eid, J. G. D. Hester, and M. M. Tentzeris, "5G as a wireless power grid," *Sci. Rep.*, vol. 11, no. 1, pp. 636(1)–636(9), Jan. 2021.
- [40] P. Bantavis, C. G. Gonzalez, R. Sauleau, G. Goussetis, S. Tubau, and H. Legay, "Broadband graded index gutman lens with a wide field of view utilizing artificial dielectrics: A design methodology," *Opt. Exp.*, vol. 28, no. 10, pp. 14648–14661, May 2020. [Online]. Available: <https://www.opticsexpress.org/abstract.cfm?URI=oe-28-10-14648>
- [41] J. Miao, "Ka-band 2 d luneburg lens design with glide-symmetric metasurface," Ph.D. dissertation, School Elect. Eng., KTH Royal Inst. Technol., 2017.
- [42] M. Ebrahimpouri and O. Quevedo-Teruel, "Ultrawideband anisotropic glide-symmetric metasurfaces," *IEEE Antennas Wireless Propag. Lett.*, vol. 18, no. 8, pp. 1547–1551, Aug. 2019.
- [43] C.-D. Diallo, "Study and design of new multibeam antenna architectures in ku and ka bands for broadband satellite communication applications," Master's thesis, Institut d'Électronique et de Télécommunications de Rennes, Université de Rennes 1, 2016.
- [44] J. Bito *et al.*, "Millimeter-wave ink-jet printed rf energy harvester for next generation flexible electronics," in *Proc. IEEE Wireless Power Transfer Conf.*, 2017, pp. 1–4.
- [45] S. Ladan, "Simultaneous wireless power transmission and data communication," Ph.D. dissertation, Département de Génie Électrique, Université de Montreal, 122014.
- [46] Q. Chen, X. Chen, H. Cai, and F. Chen, "A waveguide-fed 35-GHz rectifier with high conversion efficiency," *IEEE Microw. Wireless Compon. Lett.*, vol. 30, no. 3, pp. 296–299, Mar. 2020.
- [47] S. S. Vinnakota, R. Kumari, and B. Majumder, "Dual-polarized high gain resonant cavity antenna for radio frequency energy harvesting," *Int. J. RF Microw. Comput.-Aided Eng.*, vol. 29, no. 12, 2019, Art. no. 22003. [Online]. Available: <https://onlinelibrary.wiley.com/doi/abs/10.1002/mmce.22003>
- [48] S. Chandravanshi, K. K. Katare, and M. J. Akhtar, "A flexible dual-band rectenna with full azimuth coverage," *IEEE Access*, vol. 9, pp. 27476–27484, 2021.
- [49] S. Shen, Y. Zhang, C. Y. Chiu, and R. Murch, "Directional multiport ambient RF energy harvesting system for the internet of things," *IEEE Internet Things J.*, vol. 8, no. 7, pp. 5850–5865, Apr. 2021.
- [50] A. Riaz, S. Zakir, M. M. Farooq, M. Awais, and W. T. Khan, "A triband rectifier toward millimeter-wave frequencies for energy harvesting and wireless power-transfer applications," *IEEE Microw. Wireless Compon. Lett.*, vol. 31, no. 2, pp. 192–195, Feb. 2021.
- [51] D. Matos, R. Correia, and N. Carvalho, "Millimeter-wave hybrid RF-DC converter based on a gaas chip for IoT-WPT applications," *IEEE Microw. Wireless Compon. Lett.*, pp. 1–1, 2021.